Bathymetry and absorptivity of Titan's Ontario Lacus

A. G. Hayes, A. S. Wolf, O. Aharonson, H. Zebker, R. Lorenz, R. L. Kirk, Philippe Paillou, J. Lunine, L. Wye, P. Callahan, et al.

Bathymetry and absorptivity of Titan's Ontario Lacus

A. G. Hayes,[1] A. S. Wolf,[1] O. Aharonson,[1] H. Zebker,[2] R. Lorenz,[3] R. L. Kirk,[4] P. Paillou,[5] J. Lunine,[6] L. Wye,[2] P. Callahan,[7] S. Wall,[7] and C. Elachi[7]

Received 8 December 2009; revised 2 April 2010; accepted 3 June 2010; published 23 September 2010.

[1] Ontario Lacus is the largest and best characterized lake in Titan's south polar region. In June and July 2009, the Cassini RADAR acquired its first Synthetic Aperture Radar (SAR) images of the area. Together with closest approach altimetry acquired in December 2008, these observations provide a unique opportunity to study the lake's nearshore bathymetry and complex refractive properties. Average radar backscatter is observed to decrease exponentially with distance from the local shoreline. This behavior is consistent with attenuation through a deepening layer of liquid and, if local topography is known, can be used to derive absorptive dielectric properties. Accordingly, we estimate nearshore topography from a radar altimetry profile that intersects the shoreline on the East and West sides of the lake. We then analyze SAR backscatter in these regions to determine the imaginary component of the liquid's complex index of refraction (κ). The derived value, $\kappa = (6.1^{+1.7}_{-1.3}) \times 10^{-4}$, corresponds to a loss tangent of $\tan \Delta = (9.2^{+2.5}_{-2.0}) \times 10^{-4}$ and is consistent with a composition dominated by liquid hydrocarbons. This value can be used to test compositional models once the microwave optical properties of candidate materials have been measured. In areas that do not intersect altimetry profiles, relative slopes can be calculated assuming the index of refraction is constant throughout the liquid. Accordingly, we construct a coarse bathymetry map for the nearshore region by measuring bathymetric slopes for eleven additional areas around the lake. These slopes vary by a factor of ~5 and correlate well with observed shoreline morphologies.

Citation: Hayes, A. G., et al. (2010), Bathymetry and absorptivity of Titan's Ontario Lacus, *J. Geophys. Res.*, *115*, E09009, doi:10.1029/2009JE003557.

1. Introduction

[2] Ontario Lacus, originally imaged by the Instrument Science Subsystem (ISS) in July 2004 and June 2005 [*Turtle et al.*, 2009], was Cassini's first glimpse into Titan's surface hydrocarbon inventory. With an area of 15,600 km^2, it remains the largest lake observed in the south polar region. The Visual and Infrared Mapping Spectrometer (VIMS) observed Ontario in December 2007 and spectrally confirmed the presence of liquid ethane [*Brown et al.*, 2008]. Infrared mapping of the shoreline at a resolution of 330–2500 m/pixel suggested the presence of surrounding annuli which *Barnes et al.* [2009] interpreted as evidence for changes in lake level. Recent observations by ISS in March 2009 (E. P. Turtle et al., Shoreline retreat at Titan's Ontario Lacus and Arrakis Planitia from Cassini Imaging Science Subsystem observations, submitted to *Icarus Notes*, 2010) and Radar in June/July 2009 [*Hayes et al.*, 2010] have detected shoreline recession, confirming Ontario is an active feature. *Lorenz et al.* [2009] discusses morphologic and hydrologic similarities between Ontario Lacus and Racetrack Playa, an ephemeral lake located in Death Valley National Park, CA USA. In this work, we derive the imaginary component of Ontario's complex refractive index and create a nearshore bathymetry map using a combination of radar backscatter and altimetry.

[3] Cassini has observed Ontario Lacus with multiple instruments between July 2004 and January 2010, making it the best characterized lacustrine feature on Titan. Synthetic Aperture Radar (SAR) images were acquired on June 22, 2009 (Titan flyby T57), July 8, 2009 (T58), and January 12, 2010 (T65). Closest approach altimetry observations were obtained in December 21, 2008 (T49). The SAR images have a resolution of 260–350 m/pixel and show varied shoreline morphologies including landforms similar to drowned river valleys and wave-dominated beachheads [*Wall et al.*, 2010]. Passive microwave radiometry, obtained coincident with active SAR, shows Ontario is colder than both its local

[1]Division of Geological and Planetary Sciences, California Institute of Technology, Pasadena, California, USA.
[2]Electrical Engineering, Stanford University, Stanford, California, USA.
[3]Johns Hopkins University Applied Physical Laboratory, Laurel, Maryland, USA.
[4]Astrogeology Team, U.S. Geological Survey, Flagstaff, Arizona, USA.
[5]Aquitaine Science Center of the Universe, University of Bordeaux, Floirac, France.
[6]Department of Physics, University of Rome, Tor Vergata, Rome, Italy.
[7]Jet Propulsion Laboratory, California Institute of Technology, Pasadena, California, USA.

0148-0227/10/2009JE003557

surroundings and northern counterparts, suggesting either evaporative cooling or a lower emissivity [*Wall et al.*, 2010; *Mitri et al.*, 2007]. Altimetry returns from the lake surface are specular in nature and place an upper limit of 3 mm on the root-mean square (RMS) height of any surface waves over the 100 m Fresnel zone of radar beam footprints during the December 2008 flyby [*Wye et al.*, 2009].

[4] The combination of closest-approach altimetry and high resolution SAR observations presents a unique opportunity to study Ontario Lacus. The normalized radar backscatter cross-section (σ_o) drops off exponentially with distance from shoreline. This behavior is consistent with attenuation through a deepening liquid medium and, if the local topography is known, can be used to estimate the imaginary component of the complex index of refraction (κ). The complex refractive index at microwave wavelength determines the depth to which radar waves can penetrate lakes on Titan, and is a function of liquid composition. Complex refractive indices are calculated in two areas where altimetry profiles intersect the lake shoreline. To within errors, both measurements are consistent and are bounded by the expected attenuation properties of liquid hydrocarbon at 90 K.

[5] The observed exponential fall-off in radar return is further used to estimate local bathymetric slopes in areas where the topography was not sampled by altimetry. These slopes are used to generate a coarse nearshore bathymetry map assuming that refractive properties are uniform throughout the lake. Using this method, we estimate bathymetric slopes for eleven additional areas around the lake, ranging from $(0.5–2.7) \times 10^{-3}$.

[6] We present our analysis in four parts: data reduction, model fitting, model validation, and discussion of results. Data processing steps taken for calculating lake-depth and average radar return are described in section 2. We develop the best-fit model to the reduced data in section 3, and assess the validity of the model and its sensitivity to underlying assumptions in section 4. Interpretation of model results, including morphological and compositional implications, are presented in section 5.

2. Data Reduction

[7] The Cassini RADAR measures the normalized backscatter cross-section (σ_o) of Titan's surface at 2.16 cm. The normalized backscatter cross-section is a non-dimensional quantity that describes the reflected power received by the radar. For every element on the surface, the measured power is converted into the effective area of an isotropic scattering surface that would produce the observed signal. This effective area is then divided by the imaged surface area yielding a non-dimensional σ_o value for each pixel [*Ulaby et al.*, 1982]. For a given wavelength, polarization, and incidence angle, σ_o is an intrinsic property of the surface and can be used to distinguish between different terrain models. Unfortunately single measurements, or looks, of σ_o are highly dependent on small-scale structure in the terrain, and thus temporal or spatial averaging is required before analyzing the effects of material properties or large-scale structure. For Ontario Lacus, the average σ_o as function of distance from shore is used to determine microwave absorption coefficients and determine local bathymetric slopes.

[8] Noise in measurements of σ_o have two common sources: speckle noise and instrument noise. Speckle noise is produced by mutually interfering electromagnetic waves that are scattered off of a surface that is rough on the order of the wavelength, and is thus embedded in the radar signal. Conversely, instrument noise results primarily from thermal noise in the antenna receiver, and is thus an artifact of radar signal measurement. Instrument noise is nominally subtracted during SAR processing and reported as the noise equivalent backscatter ($\sigma_o^{(ne)}$). Speckle noise for single-look data follows an exponential probability distribution of the form [*Goodman*, 1976]

$$P(\sigma_o)d\sigma_o = \left(1/\sigma_o^{(t)}\right) e^{-\sigma_o/\sigma_o^{(t)}} d\sigma_o \quad (1)$$

where $\sigma_o^{(t)}$ is the mean backscatter from the surface. Speckle noise is typically suppressed by averaging multiple looks of the same surface element. As the number of looks becomes large, $P(\sigma_o)$ approaches a normal distribution in accordance with the central limit theorem. For the T57, T58, and T65 radar observations, the number of looks varied from 1 to 4 and the average σ_o, reported after subtraction of $\sigma_o^{(ne)}$, is -22.3 ± 0.1 dB, -20.29 ± 0.03 dB and -18.25 ± 0.02 dB, respectively. This difference in average lake backscatter is not surprising given differences in incidence angle between flybys: 42°–44° for T57, 26°–32° for T58, and 21°–29° for T65. For a single look, the 95% confidence interval (CI) varies from −15.9 dB to +5.7 dB about the mean value $\sigma_o^{(t)}$; for four looks, this interval is reduced to only −5.6 dB to +3.4 dB. These intervals span the total backscatter variation observed in Ontario's nearshore region (−10 to −20 dB) and have significant probability of being below the average radar noise floor, which varies between flybys: -17.46 ± 0.04 dB for T57, -20.09 ± 0.05 dB for T58, and -18.97 ± 0.01 dB for T65. Within ~10 km of the shore, these σ_o values can be modeled as radiation penetrating a liquid layer and interacting with the lakebed [*Hayes et al.*, 2008, 2010; *Paillou et al.*, 2006, 2008b, 2008a; *Ventura et al.*, 2009].

[9] For observations with few looks, additional averaging is required to further reduce speckle noise. This is typically achieved through spatial averaging using box filters, which is reasonable assuming small spatial gradients in σ_o [*Elachi and van Zyl*, 2006]. In our study of Ontario's nearshore region, however, box filtering would average over the exponential falloff with distance from shoreline. Therefore, we modify the usual box averaging approach by using long and narrow boxes oriented parallel to shoreline (Figure 1, inset). Averaging in these along-shore bins reduces speckle noise while minimally affecting the expected exponential decay in the nearshore region. The error in estimates of the bin-averaged backscatter $\langle\sigma_o\rangle$ are calculated using a bootstrap Monte Carlo technique [*Press et al.*, 1992]. This technique involves creating a large number of synthetic data sets (1000) by randomly selecting, with replacement, values from the observed data within a given distance bin. Additionally, we calculate statistical metrics, such as the mean and skewness, for each synthetic data set. The 95% confidence interval (CI) of these distributions are reported as the error in the equivalent metrics for the observed data. After binning and averaging, $\langle\sigma_o\rangle$ exhibits normally distributed

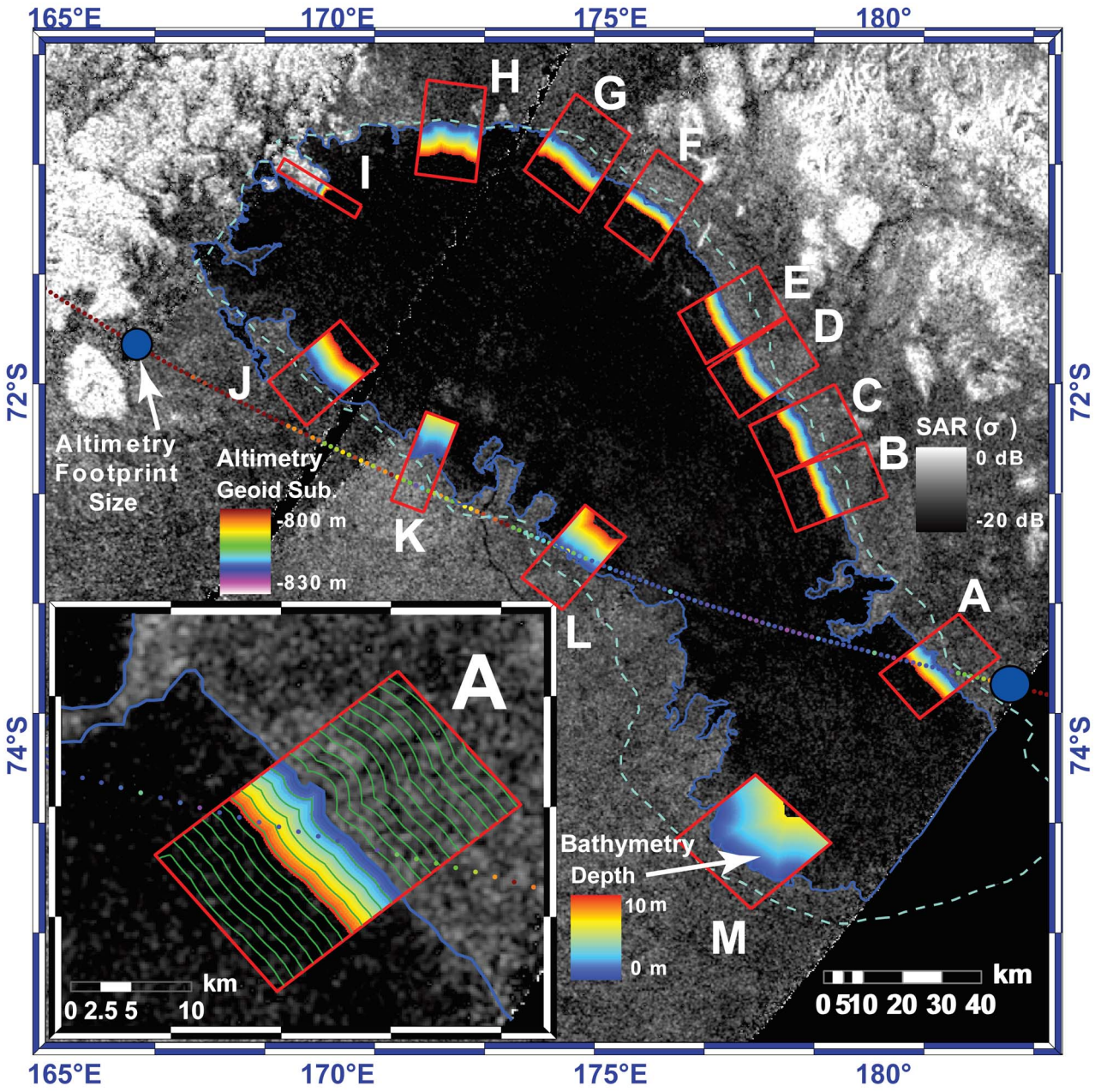

Figure 1. Equidistant cylindrical projection of Ontario Lacus centered at 72°S. Study areas A through M are outlined in red. T49 altimetry footprint centers are plotted over SAR data. Blue circles represent the size of altimetry footprints. SAR and ISS outlines of the lake are shown in blue and cyan, respectively. Nearshore bathymetry is presented within each region of interest. Regions of interest (excluding G, I, and M) are ~15 × 24 km and contain ~10^4 pixels. Regions G, I, and M have along-shore dimensions of 20, 4, and 30 km, respectively. Each distance bin contains ~10^2 pixels. Regions H, I, and J are located within T57 while the remaining regions are located in T58. Inset: Region A with contours of constant distance from shoreline. Bin size was increased by a factor of 3 as compared to analysis bin sizes for visualization purposes.

errors, enabling the use of chi-square minimization as a maximum likelihood estimator for model parameters (see section 3).

[10] In order to ensure a robust result, we calculate the distance from shore using both simple and complex shorelines. Simple shorelines are defined by two points connected by a line in the region of interest, which is 15 km in along-shore length, while the complex shorelines consist of many points with an average separation distance equal to the image resolution (260–350 m). Sensitivity to shoreline selection is not large and is discussed in section 4. Bin averaging is performed at a resolution 3 times finer than the observed data. To accomplish this, the raw data are nearest-neighbor sub-sampled to higher resolution, where depths are

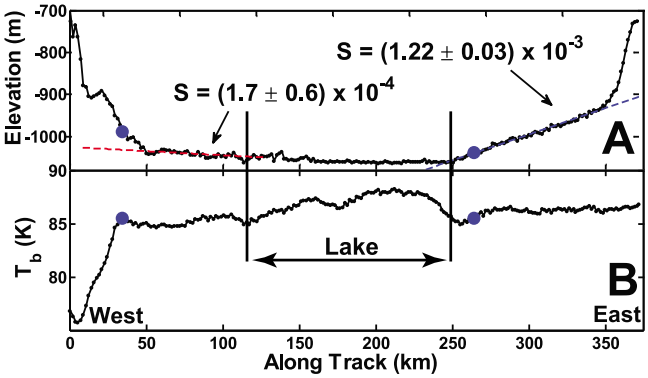

Figure 2. Analysis of December 2008 (T49) altimetry track. Blue circles correspond to positions marked in Figure 1. (a) Geoid subtracted altimetry using radar echo center of mass. Geoid values obtained from *Iess et al.* [2010]. Local slopes near altimetry intersections with Ontario Lacus are shown. (b) Brightness temperature from passive radiometry experiments. The highest value in Ontario is ~87 K, which is colder than the northern lakes.

calculated for each sub-pixel by multiplying distance from shoreline with regional slope, as discussed below. Averaging in this high-resolution space reduces artifacts introduced by finite pixel size, allowing pixels to be fractionally apportioned into appropriate depth bins.

[11] Closest approach altimetry observations obtained in December 2008 (T49) show a constant topographic slope of $S = (1.22 \pm 0.03) \times 10^{-3}$ for ~100 km leading up to Ontario Lacus (Figure 2). Assuming this measured slope extends at least a few kilometers into the lake and that the direction of steepest topographic descent is perpendicular to the shoreline, we estimate the local bathymetric slope, or dip, as $D = S/\cos\,\psi$, where ψ is the angle between the altimetry track and the local normal to shoreline. Given the bathymetric slope, we can obtain the depth of the lakebed $d = Dr$, where r is the distance from the shoreline. In the southeast altimetry intersection (region A of Figure 1) $S_A = (1.22 \pm 0.03) \times 10^{-3}$ and $\psi_A = 51.5 \pm 1.5°$. In the northwest altimetry intersection (region L of Figure 1) $S_L = (1.7 \pm 0.6) \times 10^{-4}$ and $\psi_L = 80 \pm 3°$. Correcting for orientation, the estimated bathymetric slopes are $D_A = (2 \pm 0.1) \times 10^{-3}$ and $D_L = (1 \pm 0.5) \times 10^{-3}$, similar to the topographic slopes in the lakebed of Racetrack Playa on Earth [*Lorenz et al.*, 2009]. For the remainder of this manuscript, topographic slopes will refer to measured slopes on the landward side of a shoreline while bathymetric slopes will refer to slopes in the nearshore region of a lakebed.

[12] Terrestrial examples support the assumption that nearshore bathymetry contours are parallel to lake shores and, in the absence of human intervention, are typically similar on land and lake-sides of a shoreline [*Brunskill and Schindler*, 1971; *Waples et al.*, 2005; *Gardner et al.*, 2001]. Nearshore slopes of Lake Tahoe in northeastern California, for example, are maintained for multiple kilometers away from the shore in both directions [*Gardner et al.*, 2001]. The consistent topographic slope, which extends for 100 km beginning immediately offshore of region A in Ontario Lacus, suggests that the lake lies in a shallow regional basin and that the slope would likely continue a few kilometers into the lake. This necessary assumption, while uncertain, is supported by the exponential fall-off of $\langle\sigma_o\rangle$ with distance from shore and the consistency between derived bathymetric slopes and observed morphologies (see section 5). In section 4, we test the significance of this assumption using a fractal model for small-scale topography and find that, in this case, its effects are minimal.

3. Model

[13] Together, observed SAR backscatter and estimated nearshore lake depth provide a method for measuring the complex index of refraction of Ontario Lacus. Assuming the liquid surface and lake bottom have similar backscatter properties between SAR pixels, the variation in radar-return can be described by a simple two-layer model:

$$\sigma_o^{(m)} = \sigma_o^{(1)} + \sigma_o^{(2)} e^{-8\pi\kappa d \sec\theta_{liq}/\lambda} \tag{2}$$

where κ is the imaginary component of the index of refraction and λ is the SAR wavelength in vacuum. The incidence angle in liquid hydrocarbon (θ_{liq}) is given by Snell's law:

$$\theta_{liq} = \sin^{-1}\left(n_{atm}/n_{liq}\ \sin\theta\right) \tag{3}$$

where the real components of the refractive indices for the liquid and atmosphere at 13.6 GHz are approximately $n_{liq} \approx 1.3$ and $n_{atm} \approx 1$. The three unknown parameters in this model are the combination of residual noise and backscatter from the liquid surface ($\sigma_o^{(1)}$), the lakebed backscatter at zero depth ($\sigma_o^{(2)}$), and the imaginary component of the refractive index (κ). The offset term $\sigma_o^{(1)}$ is likely composed of residual instrument noise, and any surface backscatter from Bragg waves, or other small-scale roughness on the liquid surface [*Wright*, 1968]. Small shifts in local shoreline selection primarily add an offset to lake depth affecting $\sigma_o^{(2)}$ but do not appreciably change the value of κ, which is our primary focus. It should be noted that we cannot disentangle the effects of composition and particulate scattering in the total value of κ for the liquid medium.

[14] We fit the depth-bin averaged σ_o values and their associated uncertainties to equation (1) using the Levenberg-Marquardt method for non-linear least squares estimation [*Levenberg*, 1944; *Marquardt*, 1963]. To find the best fit, we minimize the reduced chi-square fitness metric, defined as

$$\chi_\nu^2 = \frac{1}{N_{dof}} \sum_{i=1}^{N} \frac{\left(\langle\sigma_o\rangle - \sigma_o^{(m)}\right)^2}{\left(\mathrm{var}(\langle\sigma_o\rangle) + \left(\frac{\partial\sigma_o^{(m)}}{\partial d}\right)^2 \mathrm{var}(d)\right)} \tag{4}$$

where the modeled value $\sigma_o^{(m)}$ is defined by equation (2), var (x) is the variance in x, N is the number of points in the transition region, and N_{dof} is the number of degrees of freedom. Uncertainties in $\langle\sigma_o\rangle$ are estimated using the Monte Carlo routine described in section 2. Variance in depth, var(d), is controlled by the combination of errors in shoreline selection and unknown small-scale roughness of the lakebed. We fit assuming both perfect shoreline selection (var(d) = 0) and 1 pixel error in shoreline estimation

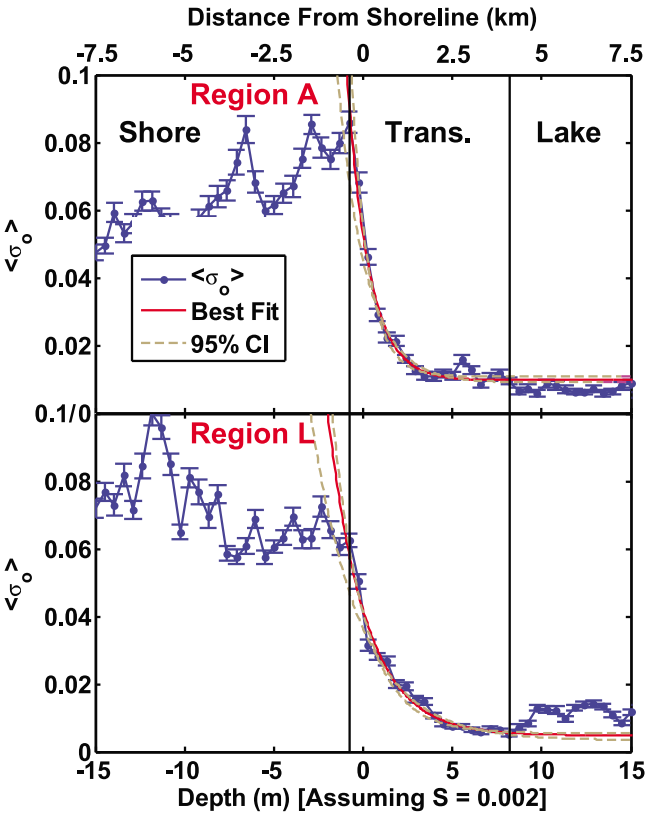

Figure 3. (top) Along-shore averaged radar backscatter and model fits for Region A. (bottom) Along-shore averaged radar backscatter and model fits for Region L. The red and brown lines represents the best-fit and 95% CI models within the transition region. Data from within the lake and on the shoreline were not used in fitting. The left-edge of the transition region was selected by hand. Zero-depth corresponds to pixels lying along the Ontario shoreline derived from image data and does not necessarily correspond to the left edge of the transition region.

(var(d) = (D Δx_{pix})^2, where Δx_{pix} is the pixel resolution which varies from 260–350 m).

[15] We estimate confidence intervals using a bootstrap Monte Carlo technique and report the maximum extent of the 95% confidence ellipses in parameter space [*Press et al.*, 1992]. Using a bathymetric dip of $(2 \pm 0.1) \times 10^{-3}$ to calculate lake-depth, we find the imaginary component of the complex index of refraction for region A (Figure 3, top) to be $\kappa_A = (6.1^{+1.7}_{-1.3}) \times 10^{-4}$. The reduced chi-square value of the fit, assuming no error in depth estimation, is $\chi^2_\nu = 5.0$. Allowing for 1 pixel errors on the distance from shoreline or equivalent vertical noise, the reduced chi-square is $\chi^2_\nu = 1.2$. Incorporating ~1 pixel errors in shoreline position does not, to within errors, alter the values of the best-fit coefficients (see section 4). Fitting the average radar return from region F, using a slope $D_L = (1 \pm 0.5) \times 10^{-3}$, the best-fit complex index of refraction is $\kappa_L = (6.2^{+3.5}_{-2.5}) \times 10^{-4}$, consistent with region A. Region L has a reduced chi-square value of $\chi^2_\nu = 9.0$ assuming perfect shoreline position and $\chi^2_\nu = 1.4$ assuming 1 pixel error in shoreline position or equivalent vertical noise. The highly oblique angle between the altimetry track and shoreline near region L, however, makes our determination of slope much more uncertain.

[16] In all regions around the lake backscatter variation can be split into three components: shore response, near-shore transition, and lake response. Figure 3 shows $\langle \sigma_o \rangle$ versus d for regions A and L plotted alongside the models for the best fit and 95% confidence intervals. The two plateaus for large distances from the transition region are the shore and lake response, respectively. We fit the two-layer model to data in the transition region, which is bounded by vertical lines. Correlated noise arising from low SNR and structure in the lake interior increases χ^2_ν when the transition region is extended further offshore. The fit error can be reduced in these regions by omitting outliers in the darkest portions of the lake. The best fit coefficients, however, are not significantly affected by this structure. Increased amplitude of the noise structure outside the transition region begins where the real aperture radar footprint includes only dark lake pixels, thus hindering echo phase determination during SAR processing.

[17] We determined fit coefficients for thirteen locations around the lake (Figure 1, regions A–M), and present results in Table 1. In regions other than A or L, where the altimetry track intersects the shoreline, the resulting exponential coefficient represents the product of the imaginary index of refraction multiplied by the ratio of the local bathymetric slope to the measured topographic slope in A. Assuming that the index of refraction does not vary around the lake, the difference in fit coefficients are equal to the relative slope, representing a coarse lake bathymetry. Morphologic correlations with variations in relative bathymetric slope are discussed in section 5.

[18] The reported model coefficients are derived using the T57 and T58 SAR data. The T65 SAR data was acquired while this manuscript was in review and the final calibration was not available at the time of publication. Preliminary analysis of T65 data, however, returns similar results for κ and bathymetric slope despite differences in viewing geometry, adding confidence to the results reported here.

4. Model Validation

[19] In order to model the observed nearshore backscatter as exponential attenuation through a deepening liquid medium, we assumed both that the shoreline is accurately determined and that bathymetric contours are parallel to the local shoreline. As shown in the previous section, we can model the observed data well using these assumptions. Nevertheless, it is important to explore how violations of these assumptions might bias our results. In the following section, we examine how errors in shore-line selection and realistic small-scale lakebed topography might affect our analysis. We demonstrate for both of these cases that error sources large enough to significantly change our results also noticeably alter the pixel brightness distribution statistics within our SAR images, imprinting them with identifiable markers. We do not find evidence for these markers in our observed data, suggesting such significant errors are not present.

[20] The variance in SAR pixel backscatter due to speckle noise confounds shoreline selection. It is thus reasonable to expect some mixing of true lake and shore pixels in the

Table 1. Model Fitting Results for Regions A–M[a]

Region	$\sigma_o^{(1)}$			$\sigma_o^{(2)}$			D ($\times 10^{-3}$)			χ^2_ν Fit	χ^2_ν LM	χ^2_ν ExM
	Mean	LCL	UCL	Mean	LCL	UCL	Mean	LCL	UCL			
A	0.009	0.0080	0.0098	0.044	0.038	0.052	2.00[b]	1.90[b]	2.10[b]	1.2	5.9	1.4
B	0.018	0.0099	0.022	0.055	0.026	0.073	2.52	0.86	3.98	2.3	3.4	2.6
C	0.023	0.015	0.027	0.049	0.027	0.064	2.29	1.25	3.71	2.6	5.2	2.7
D	0.019	0.017	0.020	0.040	0.027	0.053	2.34	1.43	4.05	14.2	9.9	3.7
E	0.016	0.004	0.019	0.039	0.021	0.107	2.23	1.33	4.62	9.92	10.9	2.8
F	0.01	0.009	0.012	0.054	0.044	0.063	2.68	2.12	3.44	8.6	9.8	3.9
G	0.009	0.0082	0.010	0.022	0.016	0.027	1.85	1.56	2.52	8.9	23.6	5.5
H	0.0056	0.0037	0.0072	0.033	0.029	0.037	1.40	0.83	1.96	8.0	47.1	6.9
I[c]	0.0097	0.0075	0.012	0.070	0.029	0.092	4.85	2.83	5.87	3.6	33.1	2.4
J	0.013	0.0046	0.021	0.026	0.018	0.036	1.24	0.71	2.16	6.5	7.0	3.4
K	0.0038	0.0014	0.007	0.056	0.047	0.065	0.74	0.60	0.88	8.7	75.0	6.9
L	0.0021	0.00056	0.048	0.041	0.037	0.046	1.00[b]	0.50[b]	1.50[b]	1.4	50.2	2.4
M	0.021	0.018	0.025	0.026	0.038	0.033	0.46	0.39	0.61	6.6	5.1	2.3

[a]Coefficient errors are the lower and upper confidence limits (LCL and UCL) of the 95% confidence interval. Local bathymetric dip (D) is determined by referencing to the observed on-land topographic dip at region A ($D_A = (2 \pm 0.1) \times 10^{-3}$) and assuming the imaginary component of the index of refraction (κ) is uniform throughout the lake. The model parameters $\sigma_o^{(1)}$ and $\sigma_o^{(2)}$ represent the surface backscatter and zero-depth lakebed backscatter as defined by equation (2) and discussed in section 3. Chi-square goodness-of-fit metrics (χ_ν) are reported for the data, Linear Mixing Model (LM), and Exponential Attenuation Model (ExM) as described in section 4.

[b]Denotes that the slopes are measured using on-land Altimetry measurements (Regions A and L) as opposed to estimated using the model coefficients.

[c]Denotes areas where there are less than four depth bins within the first two exponential skin depths of the transition region.

transition region when using an uncertain shoreline. Linear mixing of bright and dark values may imitate the expected backscatter fall-off with distance from shore. Therefore, it is important to limit the polluting effects of linear mixing by restricting our analysis to regions of low shoreline complexity (Figure 1, regions A–M). Additionally, we characterize the effects of improper shoreline selection to ensure that linear mixing is not skewing the results. This is accomplished by analyzing the shape of backscatter distributions within each depth bin. We find that small errors in shoreline selection do not significantly affect the results, and large errors can be ruled out by the changes they induce in distribution characteristics within the transition region.

[21] As a first test for the dependence of our analysis on shoreline selection, we use both straight-line (within the region of interest) and smoothly varying shorelines to calculate pixel depths. The resulting best-fit coefficients do not vary outside their error between the straight-line and smoothly varying cases, though the reduced chi-square and parameter variances for the straight-line fits are characteristically larger. In order to confidently rule out linear mixing, a more careful study was performed by comparing the data to two end-member models. The first model uses a highly complex shoreline and synthesizes images based on linear mixing alone. In the second model, we assume the backscatter in the transition region between shore and lake pixels results purely from exponential decay through a deepening liquid medium. Each model is two-dimensional and generates images that are processed using the same data reduction and modeling techniques outlined in sections 2 and 3. The characteristics of the pixel distributions for both models within each distance bin are then compared to the observed data.

[22] The Linear Mixing Model (LM) uses a complex shoreline created by following contours of σ_o around Ontario Lacus. Constant values for lake (σ_{lake}) and shore (σ_{shore}) backscatter are obtained using least squares minimization, matching the backscatter inside and outside the lake far from the transition region (Figure 3). For each distance bin, we record the extent of mixing that results from the meandering of the complex shoreline relative the smoothly varying shoreline discussed in section 3. A synthetic two dimensional image at the resolution of the SAR data is generated by assigning lake or shore identities to each pixel according to the complex shoreline, while distance bins for along-shore averaging are generated using the smooth shoreline. The backscatter of a pixel is then determined by averaging random draws from a speckle noise distribution centered at σ_{lake} or σ_{shore} (equation (1)). The number of draws are determined by the number of looks for each pixel in the original data.

[23] In contrast to LM, the Exponential Attenuation Model (ExM) assumes no linear mixing. ExM generates a two dimensional image using average backscatter values determined by the best-fit coefficients from equation (2) for the smooth shoreline defined in section 3. The purpose of ExM is to understand the expected variation in σ_o assuming exponential attenuation through a deepening liquid medium. Similar to LM, pixel values are assigned by averaging random draws from an appropriate speckle noise distribution, where the number of draws are given by the number of looks in the actual data. In order to understand noise-induced variations, each model is generated many times and the distributions of statistical metrics are recorded.

[24] While the effect of linear mixing on the average backscatter in the transition region can be similar to exponential attenuation, it causes large changes to the shape of the pixel distributions for even small degrees of contamination. One metric for the shape of a distribution is the skewness (γ_1), which is a measure of asymmetry about the mean [*Press et al.*, 1992]. For single-look observations, speckle noise skewness is 1.6–2.6 (95% CI), regardless of $\sigma_o^{(t)}$, and decreases with the square root of the total number of looks. When draws are made from two or more speckle noise distributions, such as in LM, data skewness can increase to values of 8 or greater. Skewness is most sensitive to small percentages of shore contamination in a bin mostly composed of lake pixels. Other statistical metrics, such as

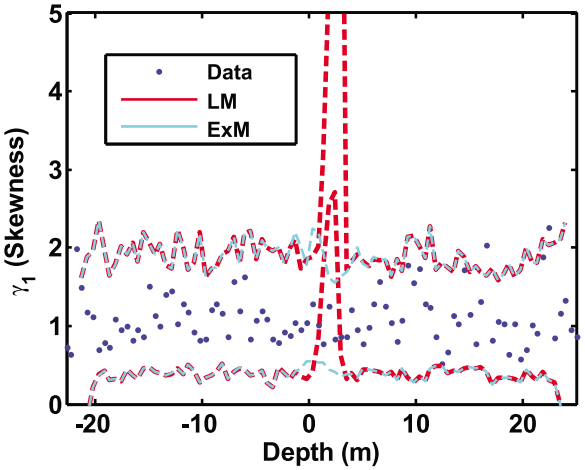

Figure 4. Skewness (γ_1) for region A. The observed data is plotted in blue. Skewness for the Linear Mixing Model (LM) and Exponential Attenuation Model (ExM) is shown in red and cyan, respectively. The lines are the lower and upper bounds of the 95% CI for each model. Note the LM shows a large increase in skewness within the transition region that is not observed in the data, or ExM. This suggests that the data does not have significant mixing of shore and lake pixels within the same distance bin.

the relative mean difference, non-uniformity, and kurtosis, are sensitive to greater percentages of contamination. Skewness in region A, for the observed data and both backscatter models, is shown in Figure 4. As expected, LM shows a large increase in skewness within the transition region. In contrast, ExM and observed data have similarly low values of skewness in all regions, suggesting that the observed data is dominated by exponential attenuation rather than linear mixing. This relationship holds true for all regions of interest.

[25] The reduced chi-square between the ExM and observed data in region A is 1.4, in agreement with the 1-D fits using equation (2). Goodness of fit between LM and observed data, however, is significantly poorer ($\chi^2_\nu = 5.9$). Reduced chi-square values comparing ExM and LM to observed data in other regions are listed in Table 1. Areas where the transition region is as narrow as 1–2 pixels, such as the northern mountainous terrain, reinforces the interpretation that exponential attenuation in variable lake depth is responsible for more gradual transitions, which can be as wide as ~40 pixels in region M.

[26] While the above test rules out pure linear mixing, it relies on a particular choice for the smooth and complex shorelines. In order to test sensitivity and error in shoreline selection, we examine adding varying amounts of noise to the nominal hand-selected shoreline position. Obtaining meaningful results, however, requires generating potential shorelines which have characteristics that are similar to the actual shoreline. We show in the following paragraphs that the traced shoreline of Ontario Lacus is well-described as a fractal, and that results are robust with respect to plausible alternate shoreline tracings generated with similar fractal character.

[27] It is well-established that natural landscapes can often be described using a fractal relationship between measurement length-scale and the amplitude of topographic variation [*Mandelbrot*, 1983; *Turcotte*, 1997]. One of the first and simplest applications of fractal analysis to natural geomorphic phenomena was the analysis of the British coastline by *Mandelbrot* [1967]. In this and many subsequent investigations [e.g., *Phillips*, 1986; *Jiang and Plotnick*, 1998; *Schwimmer*, 2008; *Sharma and Byrne*, 2008], researchers have noticed that coastlines are often found to follow an allometric relationship:

$$L(s) \propto s^{1-\mathcal{D}} \tag{5}$$

where $L(s)$ is the observed length of a section of coastline using a measure stick of length s, and $\mathcal{D}$ is the fractal dimension of the coastline. We have observed an allometric relationship for the extended smooth region of Ontario's eastern shoreline using the divider method defined in [*Klinkenberg and Goodchild*, 2006]. From Figure 5, it is clear that the shoreline trace is well described as a fractal with $\mathcal{D} = 1.095 \pm 0.003$ on length-scales between the SAR image resolution (260–350 m) and ~2 km. At length-scales larger than this crossover length, fractal behavior breaks down yielding a smooth shoreline. While we do not investigate the cause of this behavior here, it may be the result of wave action or some other erosional mechanism operating predominantly at larger length-scales.

[28] We generate fractals using the spectral method described by *Saupe et al.* [1988] in order to test model sensitivity. This method is based upon how the scale dependence of a fractal feature expresses itself in the features's power spectrum. *Saupe et al.* [1988] show that the power spectral density of a fractal curve is related to spatial frequency by a power law. Using this relation, we generate random fractals by creating power spectra of the desired spatial dimension,

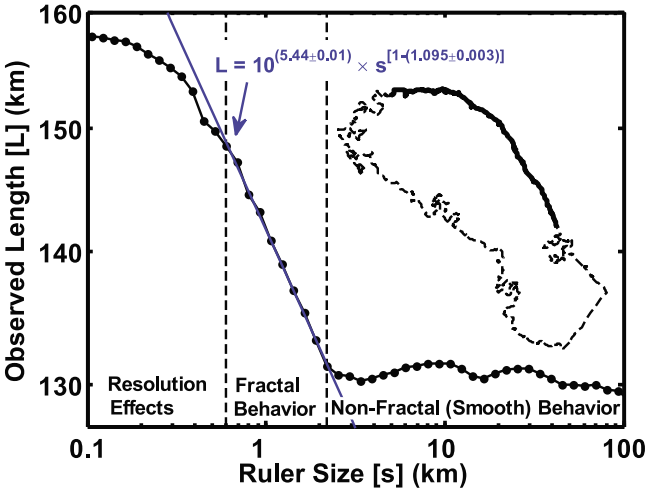

Figure 5. Allometric relationship between ruler size (s) and observed length (L) for the eastern shore of Ontario Lacus. Fractal behavior is observed between SAR image resolution (few hundred meters) and $s \sim 2$ km with a fractal dimension $\mathcal{D} = 1.095 \pm 0.003$. The analyzed section of Ontario's shoreline is shown in bold on the dashed outline.

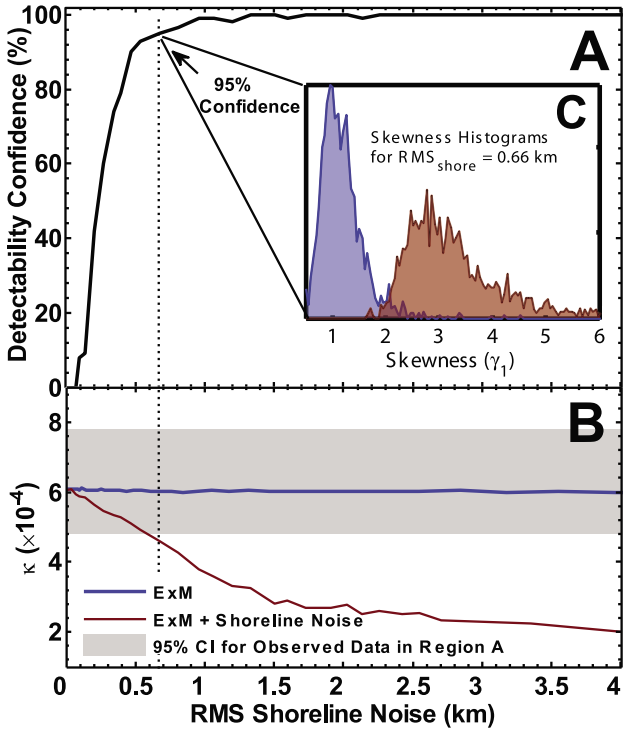

Figure 6. Effect of shoreline selection for region A. Abscissa denote RMS half-amplitudes of fractal error introduced into the shoreline position. Peak half-amplitudes are approximately twice the RMS. Pixel scale varies from 280–350 m. (a) Detectability confidence, defined as the fraction of analysis runs for which transition region skewness is outside the 95% CI of the expected distribution from exponential attenuation. (b) Best-fit imaginary refractive index (κ) derived using the noise modified shoreline. The mean κ (red line) remains above the lower 95% CI for 0 shoreline error for up to 90% detectability confidence, suggesting minimal error contribution from mixing in the reported $\kappa = (6.1^{+1.7}_{-1.3}) \times 10^{-4}$. (c) Distribution of skewness values from model runs with 0 and 0.67 km RMS shoreline noise (95% detectability confidence).

and then apply an inverse fourier transform after randomizing the phases of each frequency. This procedure is applied down to the fractal crossover of ~2 km, with zero power at lower frequencies. In the following paragraphs, we use this method in one and two dimensions in order to explore model sensitivity to shoreline selection and small-scale lakebed topography.

[29] Sensitivity to shoreline selection is studied using one-dimensional fractals as realistic noise sources added perpendicular to the local shoreline trend. Alongshore-averaged backscatter and best-fit parameters to equation (2) are evaluated using distance bins recalculated for the new shoreline. The calculation is repeated 100 times for each noise amplitude. Figure 6a shows the percentage of shoreline models whose skewness values are inconsistent with exponential attenuation in region A. For shorelines with RMS noise amplitudes >0.7 km, 95% of the models are inconsistent with ExM, requiring draws from multiple $\sigma_o^{(t)}$ distributions. Pixel resolution varies from 280–350 m in range and 260–280 m in azimuth, suggesting shorelines were selected to better than ~2 pixel accuracy. The best-fit imaginary refractive index (Figure 6b), which decreases with added shoreline noise, varies only slightly below the lower bound of its 95% CI over this region (4.6 vs. 4.8 × 10^{-4} for 95% detectability confidence, see Figure 6). LMs generated using the artificially noisy shorelines have large skewness, similar to Figure 4, and are hence all distinguishable from exponential attenuation. While we do not perform a double-blind control experiment to simulate shoreline selection biases, our method of adding synthetic noise provides a reasonable representation that offers the advantage of numerical convenience and speed.

[30] In addition to assuming accurate shoreline selection, we also assume that bathymetry contours are parallel to the local shoreline. The amplitude of small-scale variations in lakebed depth, which result in deviations from this assumption, are the second primary source of error in our analysis. Speckle noise prevents measuring small-scale variations in lakebed topography from σ_o itself, thus we investigate its effects using two-dimensional fractal surfaces which are added to an average local slope. After generating the surfaces, we test how the power spectral slope of the topographic model relates to the fractal character of its shoreline using a range of noise amplitudes and slope magnitudes. We find that if the underlying topography model is assumed to be fractal up to the crossover length-scale, we can easily detect this as a break in fractal slope of the shoreline as is observed for Ontario. Conversely, when we generate topographic models that are fractal at all length-scales, we find no break in slope for the corresponding shoreline. This suggests that the underlying topographic deviations from the local slope in the nearshore region of Ontario likely contains a fractal crossover at ~2 km, which can also be verified visually. We adopt a practical approach of utilizing a range of topographic models with spectral slopes and amplitudes that result in shorelines with fractal dimensions that bracket the observed value for Ontario's eastern shore. While the actual fractal dimension of the topography surrounding Ontario is interesting and may warrant further investigation, we do not attempt to study it here. Instead, the fractal model is solely used to verify the validity of our assumptions against reasonable topographic variations.

[31] Using a fractal surface to approximate topographic noise, we now test our sensitivity to local variations in lake-depth. Topographic models are generated by adding constant local slopes to fractal noise surfaces with varying amplitude and a fractal crossover at 2 km. We perform this test using a range of model surfaces whose shoreline fractal dimensions brackets that observed for Ontario. For each model, SAR images are generated using backscatter values determined from equation (2) with the best-fit coefficients for region A and a high-resolution depth map from the fractal noise model. After adding speckle noise, images are analyzed using the same process described in sections 2 and 3 by assuming that depth bins lie parallel to the local shoreline. For each model, we assess how added topographic noise affects both the best-fit parameters and recorded statistical metrics in each depth-bin. For the topographic model which best approximates the fractal character of Ontario's eastern shore, we find that the best-fit value for κ does not

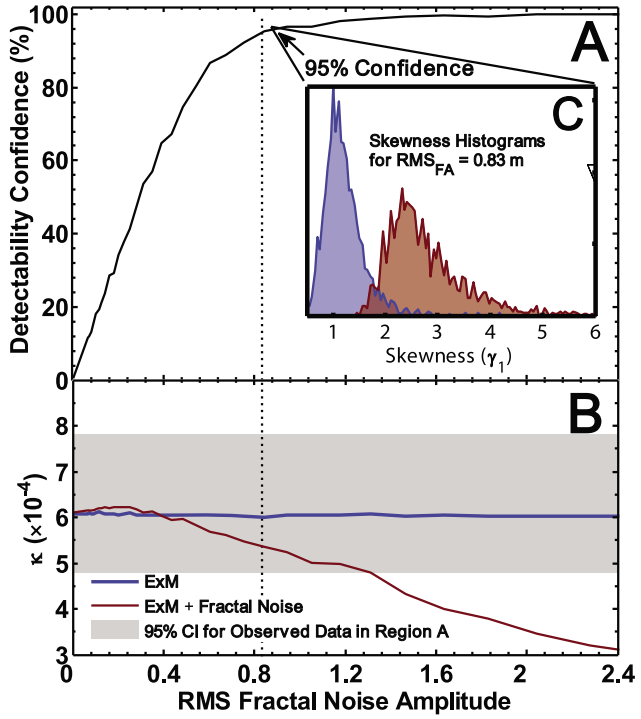

Figure 7. Effect of small-scale topography for region A. Abscissa denote RMS half-amplitudes of added fractal noise. Peak amplitudes are approximately five times the RMS. The noise amplitude for which there is a 95% probability of detecting an anomalous skewness is shown. (a) Detectability confidence, defined as the fraction of analysis runs for which transition region skewness is outside the 95% CI of the expected distribution from exponential attenuation assuming smooth topography. (b) Best-fit imaginary refractive index (κ) using σ_o derived from fractal topography. The mean κ remains above the lower 95% CI of the observed data for up to 95% Detectability confidence, suggesting minimal error contribution from small-scale topography in the reported $\kappa = (6.1^{+1.7}_{-1.3}) \times 10^{-4}$. (c) Distribution of skewness values from models runs using 0 and 0.83 m RMS amplitudes (95% detectability confidence).

vary outside its observed 95% CI for RMS noise amplitudes of up to 0.83 m (Figure 7). For larger noise amplitudes, there was greater than a 95% probability that skewness values of depth-bins in synthetic SAR images would be greater than the upper 95% CI of those generated by ExM. For other topographic models, the noise amplitude for 95% detectability confidence (Figure 7 caption) varied slightly, but the best-fit values of κ never exceeded the observed 95% CI prior to crossing this threshold. This suggests that small-scale variation in lakebed backscatter would produce detectable increases in skewness before affecting the best-fit value of κ.

[32] In summary, the combination of differences in skewness and residual chi-square favor backscatter values dominated by exponential attenuation in a deepening liquid medium, as opposed to either linear mixing or significant small-scale topographic deviation from a smooth plane. When the amount of linear mixing or amplitude of small-scale lakebed topography becomes large enough to significantly impact the derived model parameters, the skewness of pixel distributions in the transition region becomes identifiably large. These results justify the simplifying assumptions of accurate shoreline determination and bathymetry contours which are parallel to the local shoreline. The correlation between relative slope and shoreline morphology, discussed in section 5, also provides a consistency check of our analysis.

5. Discussion

[33] In this work we find the first empirical estimate of the imaginary dielectric properties of liquid hydrocarbons on Titan using Cassini observations. Assuming a real dielectric constant of 1.75 for liquid hydrocarbon [*Paillou et al.*, 2008a], the complex index of refraction of region A corresponds to a loss tangent $\tan\Delta = (9.2^{+2.5}_{-2.0}) \times 10^{-4}$ ($\tan\Delta \approx \frac{2k}{\sqrt{\epsilon_r}}$, where ϵ_r is the real component of the dielectric constant). This value is consistent with experimental measurements of liquid natural gas (LNG) at 13 GHz ($\tan\Delta_{LNG} = 1.1 \times 10^{-3}$) [*Paillou et al.*, 2008a] and the 10^{-3} upper limit for ethane and methane loss tangents at 1.2 GHz calculated by *Sen et al.* [1992]. LNG is primarily composed of methane (>90%), with smaller amounts of higher order hydrocarbons. The measured loss tangent is inversely proportional to the average effective topographic slope, or dip, at the intersection with the altimetry profile near region A ($D_A = (2 \pm 0.1) \times 10^{-3}$), and is consistent with a bulk composition of liquid hydrocarbons. More finely resolved along-track altimetry profiles may reveal slope breaks in the shoreline setting; such variations in slope would proportionally affect the best-fit value for κ and derived bathymetric slopes (P. Ford, personal communication, 2010). The low value determined for the loss tangent suggests that Ontario's margins do not have large amounts of suspended absorptive material, such as tholin ($\tan\Delta \sim 2 \times 10^{-2}$ [*Paillou et al.*, 2008a]).

[34] Reported values for κ and other model coefficients assume that nearshore lakebed backscatter ($\sigma_o^{(2)}$) does not significantly vary within the regions of interest. The observed exponential drop-off in backscatter supports this assumption, as variations in $\sigma_o^{(2)}$ would disrupt this trend. In addition, changes in study region size does not alter the best-fit model coefficients, adding further support. Last, $\langle\sigma_o\rangle$ values just outside Ontario's shoreline do not significantly vary within the any of the regions of interest. Given the observations of shoreline recession (Turtle et al., submitted manuscript, 2010; *Hayes et al.* [2010]), these regions may represent previous lakebed surfaces. However, areas of high backscatter are observed within Ontario Lacus in both T57/T58 and T65 (Figure 1). These features are located far from the study areas and suggest that Ontario is shallower or has significantly brighter lakebed in these regions.

[35] The composition of Titan's lakes is likely a mixture of ethane, methane and propane, with smaller abundances of nitrogen and higher order hydrocarbons/nitriles [*Cordier et al.*, 2009; *Lunine et al.*, 1983]. Assuming thermodynamic equilibrium at 90K, the methane to ethane ratio of a surface lake is 1:8 [*Cordier et al.*, 2009]. For a raindrop or recently precipitated liquid body, the expected composition

is 25% nitrogen and 75% methane [*Lorenz*, 1993]. While VIMS spectra confirm the presence of liquid ethane in Ontario [*Brown et al.*, 2008], the instrument was incapable of estimating its abundance or distinguishing liquid from atmospheric methane. Measurements of the cryogenic microwave optical properties of pure methane and ethane, in additional to other Titan relevant materials, are in development (M. Barmatz and K. L. Mitchell, personal communication, 2009). When these measurements become available, the complex dielectric constant of various mixtures can be compared to the observed loss tangent of Ontario Lacus, providing tests for the predicted liquid compositions.

[36] In areas where Ontario's shore does not intersect the T49 altimetry track, the coefficients of equation (2) can be used to estimate local bathymetric slope, assuming uniform refractive properties for the liquid. Along the eastern shore of Ontario (regions B, C, D, E, F), bathymetric slopes are consistent within errors and similar to the measured topographic slope at A (mean values of (2.2–2.7) $\times$ 10^{-3} vs. 2.0 $\times$ 10^{-3}, see Figure 1 and Table 1). In this area, the shoreline is smooth and morphologically similar to a beachhead modified by either persistent wave action or periodic oscillation in lake level [*Wall et al.*, 2010]. West of region F, bathymetric slopes shallow slightly (regions G and H) prior to increasing as the shoreline approaches intersection with the bright mountainous terrain which forms its northernmost borders. In most of this area the transition region is of order 1 pixel, hindering analysis and suggesting bathymetric slopes greater than 0.1 ($\sim\frac{d_{\text{trans.}}}{\Delta x_{\text{pix}}}$). The best-fit slope in region I, the only region in the area with a smooth shoreline segment and relatively low skewness, was $D_{\text{I}} = (4.8^{+1.0}_{-2.0}) \times 10^{-3}$, although only three points lie within the first two exponential skin depths. Additional measurements of topographic slope will become available after stereo processing has been completed between T57/T58 and T65 SAR observations. When this data is available, the bathymetric slopes reported in Table 1 can be compared to the nearshore topographic slopes on the landward side of Ontario's shoreline.

[37] The western shore of Ontario (regions J, K, L, and M) has shallower bathymetric slopes as compared to the eastern shore ((0.4–1.2) $\times$ 10^{-3} vs. (1.8–2.7) $\times$ 10^{-3}). This observation is consistent with the larger values of shoreline recession observed between the 2005 ISS and 2009 SAR images of this coast (Hayes et al., submitted manuscript, 2010). Region K is located near deltaic lobate structures fed by a large tributary system extending toward the lake from the West. The returned bathymetric slope near the deltaic-like features are 1.4 times lower than the effective topographic slope of $D_{\text{L}} = (1 \pm 0.5) \times 10^{-3}$, as derived from altimetry echo center-of-mass near region L. Gently sloping depth profiles near these features are consistent with a multilobe shallow-water delta created from distributary channel switching [*Wall et al.*, 2010].

[38] Region L intersects T49 and has a bathymetric slope value consistent with the topographic slope calculated using the altimetry data. The effective bathymetric slope in region M, located in Ontario's southeast corner, is 4 times shallower than the topographic slope observed at A. This region also contains a lower average $\langle\sigma_{\text{o}}\rangle$ within the lake (−14 dB ± 3 dB) and is near the largest observations of shoreline recession observed between the ISS and SAR images [*Hayes et al.*, 2010]. The inverse proportionality between local bathymetric slope and shoreline recession magnitude suggests a uniform drop in lake level.

6. Summary

[39] SAR backscatter in the nearshore region of Ontario Lacus is observed to fall-off exponentially with perpendicular distance from the local shoreline. Closest approach altimetry observations suggest that Ontario lies in a shallow regional basin with slopes ~10^{-3}. Together, these observations allow the derivation of the liquid's complex index of refraction through comparison of $\langle\sigma_{\text{o}}\rangle$ to a simple two-layer model with exponential dependence on lake depth (equation (2)). Model coefficients are derived using nonlinear least squares minimization of reduced chi-square (equation (3)). Error estimations show that the observed bathymetric slope variations are significant.

[40] The derived imaginary component of the refractive index is $\kappa = (6.1^{+1.7}_{-1.3}) \times 10^{-4}$ and corresponds to a loss tangent of $\tan\Delta = (9.2^{+2.5}_{-2.0}) \times 10^{-4}$, supporting the prediction that Ontario is filled with liquid hydrocarbons. This value is inversely proportional to the observed nearshore altimetric slope $D_{\text{A}} = (2 \pm 0.1) \times 10^{-3}$, consistent with previous laboratory estimates and model extrapolations of methane and ethane loss tangents, and will help constrain Ontario's liquid composition when additional laboratory data become available. Significant amounts of highly absorptive material, such as tholins, are inconsistent with the measured loss tangent. The loss tangent can also be used to translate temporal backscatter variations into depth changes within Titan's lakes.

[41] In areas where altimetry does not intersect Ontario's shore the derived model coefficients imply local slopes. Absolute bathymetric slopes are calculated for eleven areas around Ontario and a coarse bathymetry map follows by referencing to the observed on-land altimetry slopes at regions A and L (Figure 1). The relative variation in these slopes is independent of derived optical properties and altimetric profiles. Bathymetric slope values on the eastern shore, which exhibits a beachhead morphology, are characteristically steeper than the western shore, where a more complex shoreline exists. The shallowest bathymetric slope occurs in the southwestern tip of Ontario, where the greatest magnitude of shoreline recession has been observed [*Hayes et al.*, 2010]. Bathymetric slope estimations are consistent with and complement observed morphology.

[42] **Acknowledgments.** The authors would like to thank Bryan Stiles for helpful discussions and the Cassini engineering team, without whom the data presented here would not have been possible. This work was supported by the Cassini Project, managed by the Jet Propulsion Laboratory, California Institute of Technology, under a contract with NASA as well as by NASA's Graduate Student Researchers Program and the NSF Graduate Research Fellowship Program.

References

Barnes, J. W., et al. (2009), Shoreline features of Titan's Ontario Lacus from Cassini/VIMS observations, *Icarus*, *201*, 217–225, doi:10.1016/j.icarus.2008.12.028.

Brown, R. H., et al. (2008), The identification of liquid ethane in Titan's Ontario Lacus, *Nature*, *454*, 607–610, doi:10.1038/nature07100.

Brunskill, G. J., and D. W. Schindler (1971), Geography and bathymetry of selected lake basins, Experimental Lakes Area, northwestern Ontario, *J. Fish Res. Board Can.*, *28*, 139–155.

Cordier, D. C., O. Mousis, I. L. Lunine, P. Lavvas, and V. Vuitton (2009), An estimate of the chemical composition of Titan's lakes, *Astrophys. J.*, *707*, L128–L131, doi:10.1088/0004-637X/707/2/L128.

Elachi, C., and J. van Zyl (2006), *Introduction to the Physics and Techniques of Remote Sensing*, 2nd ed., Wiley-Interscience, Hoboken, N. J.

Gardner, J. V., et al. (2001), Multibeam mapping of Lake Tahoe, California-Nevada from field activity: L-1-98-lt, *Tech. Rep.*, U.S. Geol. Surv. Coastal Mar. Geol., Menlo Park, Calif.

Goodman, J. W. (1976), Some fundamental properties of speckle, *J. Opt. Soc. Am.*, *66*, 1145–1150.

Hayes, A. G., et al. (2008), Hydrocarbon lakes on Titan: Distribution and interaction with a porous regolith, *Geophys. Res. Lett.*, *35*, L09204, doi:10.1029/2008GL033409.

Hayes, A. G., et al. (2010), Transient surface liquid in Titan's polar regions from Cassini, *Icarus*, in press.

Iess, L., N. J. Rappaport, R. A. Jacobson, P. Racioppa, D. J. Stevenson, P. Tortora, J. W. Armstrong, and S. W. Asmar (2010), Gravity field, shape, and moment of inertia of Titan, *Science*, *327*, 1367–1369, doi:10.1126/science.1182853.

Jiang, J., and R. Plotnick (1998), Fractal analysis of the complexity of United States coastlines, *Math. Geol.*, *30*, 535–546, doi:10.1023/A:1021790111404.

Klinkenberg, B., and M. F. Goodchild (2006), The fractal poperties of topography: A comparison of methods, *Earth Surf. Processes Landforms*, *17*, 217–234.

Levenberg, K. (1944), A method for the solution of certain problems in least-squares, *Q. Appl. Math.*, *2*, 164–168.

Lorenz, R. D. (1993), The life, death and afterlife of a raindrop on Titan, *Planet. Space Sci.*, *41*, 647–655, doi:10.1016/0032-0633(93)90048-7.

Lorenz, R. D., B. Jackson, and A. G. Hayes (2009), Racetrack and Bonnie Claire: Southwestern US playa lakes as analogs for Ontario Lacus, Titan, *Planet. Space Sci.*, *58*, 724–731, doi:10.1016/j.pss.2009.05.012.

Lunine, J. I., D. J. Stevenson, and Y. L. Yung (1983), Ethane ocean on Titan, *Science*, *222*, 1229–1230, doi:10.1126/science.222.4629.1229.

Mandelbrot, B. (1967), How long is the coast of Britain? Statistical self-similarity and fractional dimension, *Science*, *156*, 636–638.

Mandelbrot, B. (1983), *The Fractal Geometry of Nature*, W. H. Freeman, New York.

Marquardt, D. (1963), An algorithm for least-sqaures estimation of nonlinear parameters, *SIAM J. Appl. Math.*, *11*, 431–444.

Mitri, G., A. P. Showman, J. I. Lunine, and R. D. Lorenz (2007), Hydrocarbon lakes on Titan, *Icarus*, *186*, 385–394, doi:10.1016/j.icarus.2006.09.004.

Paillou, P., M. Crapeau, C. Elachi, S. Wall, and P. Encrenaz (2006), Models of synthetic aperture radar backscattering for bright flows and dark spots on Titan, *J. Geophys. Res.*, *111*, E11011, doi:10.1029/2006JE002724.

Paillou, P., J. Lunine, G. Ruffié, P. Encrenaz, S. Wall, R. Lorenz, and M. Janssen (2008a), Microwave dielectric constant of Titan-relevant materials, *Geophys. Res. Lett.*, *35*, L18202, doi:10.1029/2008GL035216.

Paillou, P., et al. (2008b), Microwave dielectric constant of liquid hydrocarbons: Application to the depth estimation of Titan's lakes, *Geophys. Res. Lett.*, *35*, L05202, doi:10.1029/2007GL032515.

Phillips, J. D. (1986), Spatial analysis of shoreline erosion, Delaware Bay, New Jersey, *Ann. Assoc. Am. Geogr.*, *76*, 50–62.

Press, W., B. Flannery, S. Teukolsky, and W. Vetterling (1992), *Numerical Recipes in C: The Art of Scientific Computing*, Cambridge Univ. Press, Cambridge, U. K.

Saupe, D. (1988), Algorithms for random fractals, in *The Science of Fractal Images*, pp. 71–113, Springer, New York.

Schwimmer, R. A. (2008), A temporal geometric analysis of eroding marsh shorelines: Can fractal dimensions be related to process?, *J. Coastal Res.*, *24*, 152–158.

Sen, A. D., V. G. Anicich, and T. Arakelian (1992), Dielectric constant of liquid alkanes and hydrocarbon mixtures, *J. Appl. Phys.*, *25*, 512–521.

Sharma, P., and S. Byrne (2008), Constraints on Titan's topography through fractal analysis of shorelines, *Lunar Planet. Sci.*, *XXXIX*, Abstract 2145.

Turcotte, D. L. (1997), *Fractals and Chaos in Geology and Geophysics*, Cambridge Univ. Press, Cambridge, U. K.

Turtle, E. P., J. E. Perry, A. S. McEwen, A. D. DelGenio, J. Barbara, R. A. West, D. D. Dawson, and C. C. Porco (2009), Cassini imaging of Titan's high-latitude lakes, clouds, and south-polar surface changes, *Geophys. Res. Lett.*, *36*, L02204, doi:10.1029/2008GL036186.

Ulaby, F. T., R. K. Moore, and A. K. Fung (1982), *Microwave Remote Sensing: Active and Passive*, vol. 2, Artech House, Norwood, Mass.

Ventura, B., C. Notarnicola, D. Casarano, M. Janssen, and F. Posa (2009), Characterization of Titan surface scenarios combining Cassini SAR images and radiometry data, paper presented at General Assembly 2009, Abstract EGU2009-13070, Eur. Geophys. Union, Vienna.

Wall, S., et al. (2010), Active shoreline of Ontario Lacus, Titan: A morphological study of the lake and its surroundings, *Geophys. Res. Lett.*, *37*, L05202, doi:10.1029/2009GL041821.

Waples, J., R. Paddock, J. Janssen, D. Lovalvo, B. Schulze, J. Kaster, and J. Klump (2005), High resolution bathymetry and lakebed characterization in the near-shore of western Lake Michigan, *J. Great Lakes Res.*, *31*, 64–74.

Wright, J. W. (1968), A new model for sea clutter, *IEEE Trans. Antennas Propag.*, *16*, 217–223.

Wye, L. C., H. A. Zebker, and R. D. Lorenz (2009), Smoothness constraints on Titan's Ontario Lacus: Constraints from Cassini RADAR specular reflection data, *Geophys. Res. Lett.*, *36*, L16201, doi:10.1029/2009GL039588.

O. Aharonson, A. G. Hayes, and A. S. Wolf, Division of Geological and Planetary Sciences, MC 150-21, California Institute of Technology, Pasadena, CA 91125, USA. (hayes@gps.caltech.edu)

P. Callahan and S. Wall, Jet Propulsion Laboratory, MS 179-224, 4800 Oak Grove Dr., Pasadena, CA 91109, USA.

C. Elachi, Jet Propulsion Laboratory, MS 180-904, 4800 Oak Grove Dr., Pasadena, CA 91109, USA.

R. L. Kirk, Astrogeology Team, U.S. Geological Survey, 2255 N. Gemini Dr., Flagstaff, AZ 86001, USA.

R. D. Lorenz, Johns Hopkins University Applied Physics Laboratory, 1100 Johns Hopkins Rd., Laurel, MD 20723, USA.

J. Lunine, Department of Physics, University of Rome, Tor Vergata, I-00173 Rome, Italy.

P. Paillou, Aquitaine Science Center of the Universe, University of Bordeaux, 2 rue de l'Observatoire, BP 89, F-33270 Floirac, France.

L. Wye and H. Zebker, Electrical Engineering, MC 9515, Stanford University, Stanford, CA 94305, USA.